

# Optimization of Comb-Driven Devices for Mechanical Testing of Polymeric Nanofibers Subjected to Large Deformations

Mohammad Naraghi and Ioannis Chasiotis, *Member, ASME*

**Abstract**—Comb-driven electrostatic actuators applied to mechanical testing of nanostructures are usually designed by a “brute-force” approach for maximum electrostatic-force output, which results in limited actuation range. This issue is more prevalent when testing soft nanofibers with large ductility. In this paper, the design considerations for a comb-driven platform for nanoscale mechanical testing of ductile nanofibers subjected to 50%, or larger, inelastic extensions are presented. The optimization carried out aimed at increasing the net-force output by comb drives with clamped-clamped tethers, which also improves on the accuracy in the calculation of the force that is applied onto the nanofiber specimens. At large actuator motions, tethers of low bending stiffness increased the net force applied to a nanofiber and provided better accuracy in the calculation of the applied force. On the contrary, at small actuator motions, the maximum net-force output by the comb drives increased with the axial tether stiffness due to the associated increase in the pull-in-instability voltage. The fabricated surface-micromachined devices enabled experiments with individual electrospun polyacrylonitrile nanofibers at a maximum force of 30  $\mu\text{N}$  and extensions up to 60%. The force output calculated from the voltage input to the electrostatic devices was compared to direct measurements by an independent optical method. [2008-0252]

**Index Terms**—Measurement, microelectromechanical devices.

## NOMENCLATURE

$eff$	Comb-drive force efficiency [defined in (13)].
$g$	Gap between the interdigitated comb fingers.
$h$	Device thickness.
$I$	Second moment of area for in-plane bending of the tethers.
$l$	Length of the tethers.
$l_f$	Comb-finger length.
$l_i$	Initial overlap of the comb fingers.
$n_t$	Number of tethers for each device.
$w$	Width of the tethers.

$x$ -direction	Parallel to the longest edge of comb-drive fingers. This is also the direction of actuation of comb drives, the direction of nanofiber extension, and the direction of the lateral deflection of the supporting tethers (see Fig. 1).
$y$ -direction	Perpendicular to the longest edge of comb-drive fingers. This is also the direction of the lateral motion of comb drives and the direction of the axial deformation of the supporting tethers (see Fig. 1).
$A$	Cross section of the tethers.
$E$	Elastic modulus of the tether material.
$F_E$	Total electrostatic force generated by the comb drive.
$F_{EI}$	Attractive electrostatic force between one pair of comb fingers.
$F_{\text{net}}$	Net force available to a nanofiber test specimen.
$F_t(\xi)$	Total lateral force applied in the $x$ -direction to all tethers.
$N$	Number of comb-finger pairs in each comb drive.
$P(\xi)$	Lateral force applied to each tether in the $x$ -direction.
$P_{\text{cr}}$	Buckling load of a tether in fixed–fixed configuration.
$V$	Applied voltage between comb fingers.
$V_{\text{pull-in}}$	Applied voltage at the pull-in instability.
$\delta$	Lateral deflection of the tethers.
$\delta_{\text{max}}$	Maximum deflection of the tethers.
$\epsilon_0$	Permittivity of the air.
$\lambda$	Absolute uncertainty in the measurement of the tether deflection.
$\xi$	Lateral displacement of the moving set of comb fingers.
$\xi_I$	Initial lateral offset between opposite sets of fingers.
$\xi_{\text{ins}}$	Lateral displacement of the moving set of comb fingers at the pull-in instability.
$\Delta_\lambda(\cdot)$	Uncertainty in a quantity ( $\cdot$ ) caused by an uncertainty $\lambda$ in the measurement of the tether deflection.

Manuscript received October 6, 2008; revised June 19, 2009. First published August 18, 2009; current version published September 30, 2009. This work was supported in part by the National Science Foundation (NSF) under NSF-NIRT Grant DMI-0532320 and in part by the Solid Mechanics Program on Composites for Marine Structures under ONR Grant N00014-07-1-0888, with Dr. Y. D. S. Rajapakse as the Program Manager. Subject Editor S. M. Spearing.

M. Naraghi is with the Department of Mechanical Engineering, Northwestern University, Evanston, IL 60208 USA (e-mail: naraghi2@illinois.edu).

I. Chasiotis is with the Department of Aerospace Engineering, University of Illinois at Urbana–Champaign, Urbana, IL 61801 USA (e-mail: chasioti@uiuc.edu).

Color versions of one or more of the figures in this paper are available online at <http://ieeexplore.ieee.org>.

Digital Object Identifier 10.1109/JMEMS.2009.2026944

## I. INTRODUCTION

**A**DVANCES in synthesis of nanofibers and nanowires with submicrometer diameters have opened new horizons in

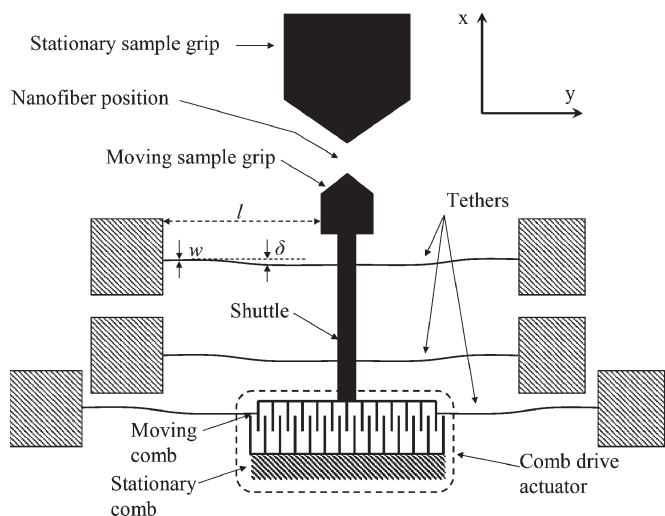


Fig. 1. Schematic of a MEMS nanofiber testing platform with a comb-drive actuator.

hierarchical materials research [1]–[5]. In particular, nanofibers with uniform diameter can be mass produced by electrospinning, which has been applied to a variety of polymers. As expected, for a polymeric material, the mechanical properties of these nanofibers are largely unknown and a strong function of the fabrication conditions.

A common approach in investigating the mechanical behavior of individual nanofibers and nanowires is single-fiber tension experiments [6]–[13]. For this purpose, complete microelectromechanical systems (MEMS), or simply microfabricated mechanical components, are very suitable, as they provide the means for precise sample mounting and alignment and, more importantly, they incorporate micromachined load cells for high resolution in force measurements. In such mechanical testing platforms, the nanofiber samples are loaded by MEMS [9]–[11] or by off-chip actuators [12], [13]. In general, on-chip actuators are preferred since they allow for accurate unidirectional sample loading, provided that they can generate sufficient forces and displacements, while their small dimensions make them appropriate for *in situ* mechanical testing inside electron microscopy chambers.

Microscale actuators that have been demonstrated in microscale tension experiments to date are surface-micromachined electrostatic [14]–[17] and electrothermal [18], [19] devices. Thermal actuators have the advantages of providing large actuation forces and being CMOS compatible. However, they have very limited allowable displacements of only a few micrometers and involve very high temperatures (in some cases, over 1000 K) [18]. Their small output displacement is due to the small coefficient of thermal expansion (CTE) (e.g., the CTE for polysilicon is  $2.6 \text{ ppm} \cdot \text{C}^{-1}$ ). The temperature increase during device operation rules out the use of thermal actuators for testing polymeric nanofibers, which are very sensitive to temperature variations. On the other hand, electrostatic actuators such as comb drives are expected to generate forces between tens and hundreds of micronewtons and displacements in the range of  $10\text{--}20 \mu\text{m}$  [14]. These actuators were employed in microscale mechanical testing platforms before [11], [17],

[20] in a rather “brute-force” approach by incorporating very large numbers of comb-drive arrays, in which, although generating large electrostatic forces, the requirements for many suspension tethers and local failures limited their success. The focus of this paper is the optimal design of a comb drive actuator in order to perform microscale tension experiments with nanofibers that require large extensions at sustained forces. Among the different types of tethers employed in comb drives [21], only clamped–clamped tethers were used in this paper, aiming at increasing the lateral stability of the comb-finger arrays, as explained in Section II-A2.

In general, two issues arise when comb-drive actuators are not designed by taking into account the compliance of their tethers and the constitutive mechanical behavior of the specimens to be tested: 1) The comb-drive actuators cease to move beyond a certain voltage (force), and hence, they are not able to further stretch a specimen, and 2) the accuracy of the calculated net force, which is output by the device to the sample, is very low. These two issues are integral in the design of the tethers suspending the entire mechanical testing device. Tethers with higher axial stiffness increase the pull-in-instability voltage between the comb-drive fingers and, therefore, the maximum net electrostatic output force. On the other hand, axially stiffer tethers have higher lateral stiffness, resulting in the reduction of the net force exerted onto a test sample. This reduction in the net output force should be considered in the design of comb drives for large travel.

In general, longer tethers reduce the fraction of the total force that is consumed by them. However, when these tethers support the moving comb fingers directly, as will be shown in this paper, the total length of the suspended structure (i.e., the tethers and the freestanding comb-finger array) is several millimeters, which reduces the yield of functioning devices after etching of the sacrificial layers and application of critical-point drying. Therefore, the tethers’ length in this paper was limited to  $l = 500 \mu\text{m}$ , which resulted in suspended structures of up to 2 mm in length.

A relevant important consideration is the influence of the stiffness of the tethers on the accuracy of the calculated force that is applied to a test sample. Stiffer tethers reduce this accuracy because the force exerted onto a nanofiber by a comb drive is calculated as the difference between the total electrostatic force and the restoring force in the suspending tethers. If the tethers’ stiffness is very high, which is required to be able to produce large actuation forces, the calculated force applied to a nanofiber can be a small portion of the tethers’ force and the total electrostatic force and is therefore comparable to the experimental uncertainties.

These considerations are further complicated when experimenting with ductile nanofibers that require large comb-drive motions (nanofiber extensions) that typically exceed  $10 \mu\text{m}$ . At large comb-drive motions, a considerable portion of the total electrostatic force is absorbed by the deflecting tethers, which results in a gradual reduction of the device net output force. In addition, at large fiber extensions (i.e., tether deflections), the axial stiffness of the tethers is reduced for all types of tethers, such as folded beams [21]–[23], crab-leg beams, and clamped–clamped beams [21], resulting in a sudden pull-in

instability between the opposing sets of comb fingers and, therefore, in a reduction of the maximum force and extension available to the nanofiber. Hence, the design of microscale testing devices incorporating comb-drive actuators involves the interplay between the maximum net-force output by the device and the maximum extension that can be applied to a ductile sample.

This paper focuses on the design of a comb-driven nanofiber testing platform to maximize the net output force to a polymeric nanofiber that is subjected to large extensions ( $> 50\%$ ) before the lateral instability in the comb fingers occurs. We revisit the device-geometry-related sources of instability in view of the presence of an attached nanofiber in order to determine the optimal device design that takes into account the mechanical behavior of the polymeric nanofibers at hand. To simplify this procedure, the comb-drive force efficiency was defined as the metric to design devices for maximum accuracy in the calculation of the net output force. Finally, comb-drive-based nanofiber mechanical testing platforms, fabricated according to the optimization guidelines discussed in this paper, were used to extract the mechanical behavior of individual polyacrylonitrile (PAN) nanofibers.

## II. ACTUATOR DESIGN FOR NANOFIBER TESTING

A basic layout of a MEMS mechanical testing platform employing a comb-drive actuator to induce deformation to a nanofiber is shown in Fig. 1. It follows a common design [11], [17] of two opposing grips for fiber mounting in-line with a comb-drive actuator. The total comb-drive output force is balanced by the tether spring force and the force exerted onto a test specimen, which are loaded in parallel. In order to prevent electrostatic attraction between the substrate and the moving parts leading to stiction of the device to the substrate, the moving part of the actuator and the substrate are kept at the same potential.

The driving attractive electrostatic force  $F_{El}$  between one pair of comb fingers is

$$F_{El} = \frac{h\varepsilon_0 V^2}{2g} \quad (1)$$

where  $h$ ,  $g$ , and  $V$  are the device thickness, the gap between the interdigitated comb fingers, and the applied voltage between them, respectively, and  $\varepsilon_0$  is the permittivity of the air. Due to design and fabrication considerations in surface micromachining, the ratio of  $h/g$  is limited to ten or less. As a result of (1), an actuation voltage of 100 V can generate only a force of 0.45  $\mu\text{N}$ . Therefore, a large number of comb-finger pairs  $N$  is used to generate a substantial force

$$F_E = \frac{Nh\varepsilon_0 V^2}{g}. \quad (2)$$

A significant percentage of this force is consumed by the tethers that deflect laterally during actuation, while the balance  $F_{\text{net}}$  is available to the nanofiber

$$F_{\text{net}} = \frac{Nh\varepsilon_0 V^2}{g} - n_t P(\delta) \quad (3)$$

where  $P(\delta)$  is the lateral force applied to each tether in the  $x$ -direction as a function of actuator travel length [or, equivalently, the lateral deflection of the supporting tethers ( $\delta$ )] (see Fig. 1) and  $n_t$  is the number of tethers. For example,  $n_t = 6$  in Fig. 1. In the same figure, the instantaneous change in the distance between the fiber grips and the lateral deflection of the tethers is the same and equal to  $\delta$ .

For small deflections, the force exerted on each tether,  $P(\delta)$ , is calculated by a strength-of-material analysis. When tether-beam deflections are large, as is the case here,  $P(\delta)$  can be calculated from the following two equations for the beam lateral force  $P(u)$  and deflection  $\delta(u)$  by eliminating the common variable  $u$ , which is a measure of the stress in the beam due to its lateral deflection [24]

$$P(u) = \frac{8EI(2I/A)^{\frac{1}{2}}}{l^3} u^3 \times \left( \frac{3}{2} - \frac{1}{2} \tanh^2(u) - \frac{3}{2} \frac{\tanh(u)}{u} \right)^{-\frac{1}{2}} \quad (4)$$

$$\delta(u) = 2(2I/A)^{\frac{1}{2}} (u - \tanh(u)) \times \left( \frac{3}{2} - \frac{1}{2} \tanh^2(u) - \frac{3}{2} \frac{\tanh(u)}{u} \right)^{-\frac{1}{2}} \quad (5)$$

where  $A$ ,  $l$ ,  $I$ , and  $E$  are the cross section, the length, and the second moment of area of the beam and the elastic modulus of polycrystalline silicon comprising the MEMS devices, respectively. The mechanical behavior of polycrystalline silicon in (4) and (5) is considered as linearly elastic, which has been shown before, even at strains as high as 2% [25]. At small beam deflections, (4) and (5) reduce to the solution of the Euler–Bernoulli differential equation for a beam. Other inputs such as the residual stresses were considered to be negligible in this paper as the particular fabrication process proceeds with depositing thin layers of polysilicon under alternating compressive and tensile stresses. The resulting polysilicon structures have very limited effective stress upon sacrificial release [26]. The absence of significant stresses can be verified by the absence of buckling of the long and slender tethers upon sacrificial release.

### A. Factors Limiting the Maximum Comb-Drive Output Force and Motion

Comb-drive actuators are functional until physical and/or electrical contact occurs between the stationary and moving sets of the comb fingers. Several reasons may lead to device malfunction: (a) the lateral comb-drive instability, known as “pull-in instability;” (b) the in-plane rotation/bending of the shaft connecting the moving array of a comb to its tethers, as shown in Fig. 1; and (c) actuation beyond the dielectric breakdown voltage (short circuit). In the first two modes of failure, mechanical contact leads to electrical contact, while in the last one, no mechanical contact is required. These failures limit the net output force (and the output displacement) by a comb-driven device. In this paper, the device design was performed with the first two instabilities in mind, which will be quantified in the next sections.

1) *Pull-In Instability*: This instability occurs as a result of the competition between the lateral electrostatic force and the

restoring spring force in the tethers in the  $y$ -direction according to Fig. 1. The total lateral force is [21]

$$F_E(\xi, V) = \frac{\varepsilon_0 NV^2 h(l_i + \delta)}{g^2} \times \left( \left(1 - \frac{\xi + \xi_i}{g}\right)^{-2} - \left(1 + \frac{\xi + \xi_i}{g}\right)^{-2} \right) \quad (6)$$

where  $l_i$ ,  $\xi$ , and  $\xi_i$  are the initial overlap, the lateral motion, and the initial lateral misalignment of the comb fingers, respectively. The initial lateral misalignment could be due to imperfections in surface micromachining and is often assumed to be about 5% of the finger design spacing [23]. Because of nonuniformities in the side-wall surface of the comb fingers, arising from reactive ion etching (RIE), the gap between two fingers,  $g$ , decreases from their top to their bottom surface. The value used in (6) for  $g$  is an average value. This nonuniform comb-finger width may also initiate the pull-in instability at high voltages.

Additionally, the in-plane bending of the comb fingers resulting from their mutual attraction may have a small contribution to the uncertainties in the calculation of the electrostatic force between each pair of comb fingers. If one considers comb fingers with width, length, and height of 2, 25, and 6  $\mu\text{m}$ , respectively, at a voltage of 150 V and a comb-finger overlap of 16  $\mu\text{m}$ , an estimate of the maximum lateral deflection of each comb finger is  $\sim 1\%$  of the initial gap, which has a rather negligible contribution to the accuracy of the computed electrostatic force. Therefore, the assumption that the opposite comb fingers are the equivalent to parallel-plate capacitors is reasonable in order to estimate the resulting electrostatic force.

The total axial force on the tethers,  $F_t(\xi)$ , which prevents the comb fingers from collapsing onto each other, can be calculated as in [21] by minimization of the potential energy for the axial tether deflection due to bending, also accounting for the axial deformation (compression or extension) of the beam due to the electrostatic force. These two contributions result in

$$F_t(\xi) = n_t \frac{EA/l}{1 + \frac{3\delta^2}{5l} \left\{ \frac{1}{(1-P/P_{cr})^2} - 1 \right\}} \frac{EA/l}{P} \xi \approx \frac{k_y}{1 + \frac{36}{10\pi^2} (\delta/w)^2} \xi \quad (7)$$

where  $k_y = n_t E(w h/l)$ , with  $w$ ,  $h$ , and  $l$  being the width, the thickness, and the length of the comb-drive tethers, respectively. Furthermore, a simplification was made in the last part of (7) by taking into account the buckling load for a tether that is  $P_{cr} = 4\pi^2 EI/l^2 \approx 160 \mu\text{N}$ . When this is compared to the share of the total lateral electrostatic force of  $\sim 45 \mu\text{N}$  that is carried by each of the six tether beams, which amounts to 7.5  $\mu\text{N}$ , one can safely assume that  $P \ll P_{cr}$ . The multiplication term to the transverse coordinate in (7) can be viewed as the corrected axial stiffness of the tethers for the effect of the combined transverse and axial electrostatic forces. Equation (7) was calculated by using the method in [21], which was originally derived for folded beams, but the value for  $P_{cr}$  used to derive (7) was that for fixed-fixed boundary conditions.

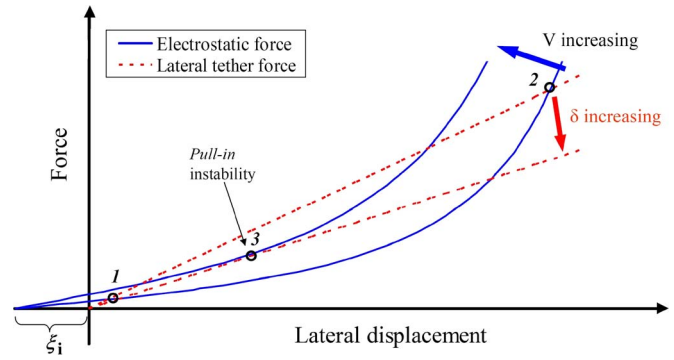


Fig. 2. Electrostatic and mechanical forces as a function of comb-finger lateral displacement in the  $y$ -direction according to the coordinates in Fig. 1.

Lateral equilibrium is maintained as long as the lateral motion of the comb fingers is suppressed by the axial force in the tethers. This condition is shown in Fig. 2, in which the two forces given in (6) and (7) are plotted as a function of lateral displacement  $\xi$  at an arbitrary lateral tether deflection  $\delta$  and actuation voltage  $V$ . At sufficiently small voltages, the two curves intersect at points 1 and 2, which are the stable and unstable equilibrium points, respectively. As the voltage increases, the electrostatic-force curve is shifted up. By increasing the bias voltage, the effective lateral stiffness of the tethers decreases due to their increased deflection  $\delta$ , as predicted by (7). As a result of these two trends, the two intersection points 1 and 2 between the solid and the dashed line move toward each other. The voltage at which the two points finally coincide is the pull-in voltage, which is point 3 in Fig. 2, when the mechanical-force curve is tangential to the electrostatic-force curve. At this point, the restoring force of the tethers still balances the electrostatic pull-in voltage, but a perturbation has a destabilizing effect resulting in the pull-in instability. At the instant of the pull-in instability, the electrostatic and the tether forces, as well as their derivatives with respect to the lateral motion (tangents), are equal [22]

$$F_E(\xi_{\text{ins}}, V_{\text{pull-in}}) = F_t(\xi_{\text{ins}}) \quad (8)$$

$$\left. \frac{\partial F_E(\xi, V_{\text{pull-in}})}{\partial \xi} \right|_{\xi=\xi_{\text{ins}}} = \left. \frac{\partial F_t(\xi)}{\partial \xi} \right|_{\xi=\xi_{\text{ins}}} \quad (9)$$

where  $\xi_{\text{ins}}$  is the tethers' lateral deflection at instability. Combining (8) and (9) gives

$$\frac{k_y}{1 + \frac{36}{10\pi^2} (\delta/w)^2} \xi_{\text{ins}} = \frac{\varepsilon_0 NV_{\text{pull-in}}^2 h \cdot (l_i + \delta)}{g^2} \times \left( \left(1 - \frac{\xi_{\text{ins}} + \xi_i}{g}\right)^{-2} - \left(1 + \frac{\xi_{\text{ins}} + \xi_i}{g}\right)^{-2} \right) \quad (10)$$

$$\frac{k_y}{1 + \frac{36}{10\pi^2} (\delta/w)^2} = \frac{2\varepsilon_0 NV_{\text{pull-in}}^2 h \cdot (l_i + \delta)}{g^3} \times \left( \left(1 - \frac{\xi_{\text{ins}} + \xi_i}{g}\right)^{-3} + \left(1 + \frac{\xi_{\text{ins}} + \xi_i}{g}\right)^{-3} \right). \quad (11)$$

Dividing (10) by (11) results in (12a), which can be solved to obtain the lateral deflection  $\xi$  of the comb drive at the pull-in instability in terms of  $g$  and  $\xi_i$

$$\frac{2\xi_{\text{ins}}}{g} = \frac{\left\{ \left(1 - \frac{\xi_{\text{ins}} + \xi_i}{g}\right)^{-2} - \left(1 + \frac{\xi_{\text{ins}} + \xi_i}{g}\right)^{-2} \right\}}{\left\{ \left(1 - \frac{\xi_{\text{ins}} + \xi_i}{g}\right)^{-3} + \left(1 + \frac{\xi_{\text{ins}} + \xi_i}{g}\right)^{-3} \right\}}. \quad (12a)$$

In this paper, we considered  $\xi_i/g = 0.05$ . Therefore,  $\xi_{\text{ins}} = 19.5\% g$  or  $\xi_{\text{ins}} \approx 400$  nm. Replacing this value of  $\xi_{\text{ins}}/g$  in (10) or (11),  $V_{\text{pull-in}}$  can be calculated as

$$V_{\text{pull-in}}^2 = 0.175 \frac{k_y}{1 + \frac{36}{10\pi^2} (\delta/w)^2} \frac{g^3}{\varepsilon_0 N h \cdot (l_i + \delta)} \quad \xi_i/g = 0.05. \quad (12b)$$

Without  $\xi_i = 0.05 g$  initial misalignment, the solution of (10) and (11) results in a zero value for  $\xi_{\text{ins}}$  at the moment of instability, which happens at the pull-in voltage

$$V_{\text{pull-in}}^2 = 0.25 \frac{k_y}{1 + \frac{36}{10\pi^2} (\delta/w)^2} \frac{g^3}{\varepsilon_0 N h \cdot (l_i + \delta)} \quad \xi_i/g = 0. \quad (12c)$$

The assumption of a 0.05-g initial misalignment underestimates the pull-in-instability voltage by about 17%. However, setting the maximum operating voltage equal to the pull-in voltage obtained from (12b), we include a safety margin against pull-in instabilities that may occur due to initial misalignments that are equivalent to 0.05 g or less.

Equation (12b) shows that the pull-in voltage is smaller for larger overlap of the comb fingers. Therefore, for design purposes, the pull-in voltage should be the upper limit for the actuation voltage that is necessary to produce the largest sample extension. In other words, the pull-in voltage can be calculated from (12b) for  $\delta = \delta_{\text{max}}$ , which is the maximum possible extension of a nanofiber. This analysis takes into account only the force and not the moment equilibrium. Placement of tethers at the root of the moving comb fingers, as shown in Fig. 1, does not allow for rotation of the shuttle, as will be pointed out in Section II-A2. Thus, the comb drive will not experience a rotational instability.

Finally, it is worth mentioning that small nanofiber misalignment between the fixed grip and the load cell is quite insignificant in terms of reducing the pull-in voltage. The moment generated by a 12–15- $\mu\text{m}$ -long nanofiber stretched with a force of 20  $\mu\text{N}$  and misaligned by 1  $\mu\text{m}$  is 20  $\mu\text{m} \cdot \mu\text{N}$ . This moment is negligible compared to the bending moment caused by the electrostatic force at the pull-in instability of about 20 000  $\mu\text{m} \cdot \mu\text{N}$ , which is estimated from an electrostatic force of 45  $\mu\text{N}$  calculated from (6) for the pull-in voltage of 200 V and a moment arm of 400  $\mu\text{m}$ , with the latter being the distance between the sample grip and the moving fingers in Fig. 1.

Finally, if the lateral pull-in instability is prevented, likely only for very short comb fingers, the pull-in instability in the  $x$ -direction at the far end of the travel of the comb drive can occur at large voltages when the tips of the moving set of fingers are sufficiently close to the root of the fixed set of fingers. This possibility can be eliminated by setting the comb fingers to be

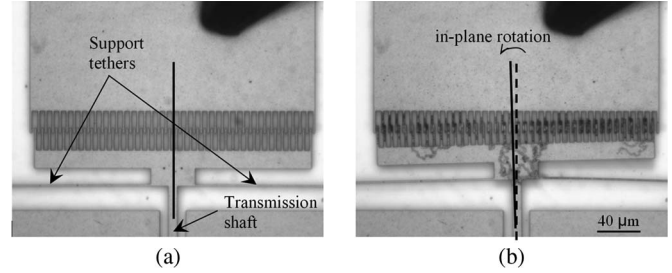


Fig. 3. Comb-drive (a) before actuation and (b) after actuation and collapse due to insufficient lateral stiffness. In this design, the tethers were not attached directly on the moving comb-finger array, as shown in Fig. 1. Premature failure was caused by the finite rotational stiffness at the point of connection between the tethers and the transmission shaft.

quite longer than the minimum travel length of the comb drive required to stretch a nanofiber to a desired strain. Therefore, the electrostatic force between the tip of the moving fingers and the root of the fixed fingers is negligible in comparison to the electrostatic forces between the sidewalls of the two sets of fingers [27].

2) *In-Plane Rotation of the Comb-Finger Support*: Insufficient lateral stiffness of the comb-drive tethers may result in rotation of the moving comb-finger array, which eventually results in contact with the stationary comb fingers, as shown in Fig. 3(b). This type of comb-drive failure occurred in devices with clamped–clamped tethers with insufficient stiffness for the applied actuation voltages. The devices in Fig. 3(a) and (b) were fabricated using the same fabrication technique employed in this paper, but the tethers were not optimized to avoid rotation at the root of the moving comb-finger array.

This failure mode, which can occur at small shuttle translations, is a result of an asymmetric lateral deflection of the tethers attached to the moving comb drive in Fig. 3(a) and (b) with respect to the shuttle axis. Failure due to moving-comb rotation is substantially prevented by increasing the in-plane stiffness of the device with wider connection shafts and by adding a pair of tethers at the root of the moving comb, as shown in Fig. 1 and later in Fig. 8(b), which does not allow for lateral comb-finger motion due to the rotation of the transmission shaft. This failure mode occurs before the pull-in instability, and therefore, its elimination allows for increased translational capacity of the comb drives.

Another factor influencing this mode of failure is the tether geometry, which is typically classified into three categories: 1) straight clamped–clamped beams; 2) crab-leg flexures; and 3) folded-beam flexures [21], [28]. In general, for the same width and length of tethers, crab-leg tethers and folded-beam flexures provide less lateral stiffness compared to straight clamped–clamped beams. This is due to the additional bending moment generated on the beams by the lateral unbalancing force  $F_E$  given by (6). Fig. 4 is instructive in this regard. This additional moment on the segments of a tether that are not parallel to the lateral force reduces the lateral stiffness of the device and finally results in lateral instability. This moment increases with actuation of the device due to an increase in the moment arm and the actuation voltage, therefore making the device less stable to external or geometrical perturbations. In order to increase the lateral stability of the MEMS test platform

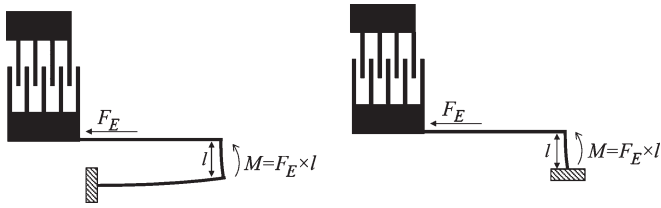


Fig. 4. Unbalancing lateral force  $F_E$  between the two opposing combs generates bending moments on (a) crab-leg-flexure-type and (b) folded-beam-flexure-type tethers, which reduces the in-plane rotational stiffness of the device and, thus, its range of operation compared to clamped-clamped beams.

described in this paper, only straight clamped-clamped tethers were considered [21].

The breakdown voltage presents the comb-driven devices with a limitation in the maximum allowable operating voltage. The average gap between the comb fingers was  $2 \mu\text{m}$ . For this value, the air ionization breakdown voltage, as described by Paschen's law, is almost  $1000 \text{ V}$  [29], which does not represent a limiting factor in the present case (actuation voltage  $< 200 \text{ V}$ ). However, there are additional mechanisms that cause dielectric breakdown in small gaps, such as field emission at voltages that are smaller than those predicted by Paschen's law [30], [31]. These voltage breakdown phenomena affect the accuracy of (12b), but they play a rather insignificant role in our measurements. For instance, in a particular device design, we observed the pull-in instability at  $V_{\text{pull-in}} \approx 180 \text{ V}$ , which was slightly lower than the prediction of  $V_{\text{pull-in}} = 200 \text{ V}$ . This small overestimate could have also stemmed from imperfections in the photolithographic patterning and RIE of the comb fingers generating tapered walls, which could have resulted in local charge buildup.

### B. Optimization of Device Geometry

Optimization of the geometry of the nanofiber testing devices was conducted having in mind the expected mechanical response of the PAN nanofibers, which, after yielding, are subjected to large extensions under relatively constant force. Table I shows the parameters that were considered as constants in the optimization procedure. Some dimensions, such as the comb-finger length  $l_f$ , the gap between fingers  $g$ , the device thickness  $h$ , and the initial overlap of the comb fingers  $l_i$ , were fully controlled by fabrication and processing optimization, such as the polysilicon-film residual stresses [32], the sacrificial-layer height, and the minimum linewidth. The rest of the device geometry parameters were calibrated according to the effective nanofiber stiffness and the nanofiber material constitutive law, i.e., the stress-strain curve of the nanofibers [12], [13]. The limiting design parameters were the ratio of device/nanofiber stiffness that changes with the deflection of the supporting tethers and the nonlinear stiffness of the nanofiber. The mechanical behavior of the nanofibers was considered as elastic-perfectly plastic [13], with a yield strain of  $\sim 5\%$  and a maximum fiber strength in the range of  $25 \mu\text{N}$ . Considering the limitations of comb drives in generating large motions, short nanofibers with gauge length of  $12 \mu\text{m}$  were selected. In practice, the fibers were mounted in a loose configuration

TABLE I  
DEVICE DESIGN CONSTANTS AND NANOFIBER PROPERTIES

Fixed design parameters	Value
Finger length ( $l_f$ )	$25 \mu\text{m}$
Gap between fingers ( $g$ )	$2 \mu\text{m}$
Device height ( $h$ )	$6 \mu\text{m}$
Initial overlap between comb-fingers ( $l_i$ )	$5 \mu\text{m}$
Fiber yield strain	$5 \%$
Maximum fiber strength	$25 \mu\text{N}$
Maximum fiber extension	$10 \mu\text{m}$ , ( $>60\%$ eng. strain)

to avoid prestress, and therefore, the initial fiber length was a few micrometers more than the distance between the unloaded grips. As a result, the maximum engineering strain was  $50\%$ – $60\%$ . For each test, the initial fiber length was measured after the fiber was straightened by an applied load via optical microscopy and with a resolution of about  $300 \text{ nm}$ .

The optimized comb drives were aimed at satisfying two criteria: 1) Generate sufficient force and motion to deform the ductile nanofibers to large strains and 2) provide the maximum possible accuracy in determining the net force applied onto the nanofibers by simply calculating the total electrostatic force generated by the comb fingers under applied voltage  $V$ , and the force stored in the tethers due to their lateral deflection. The first criterion was met by designing comb drives that, according to (3), could generate simultaneously the force and the motion specified in the last two rows of Table I, respectively, prior to the pull-in instability.

While the relevance to the first criterion for comb-drive design is evident, the latter requires further explanation. The second criterion is tied to the ability of the device to transmit the largest fraction of the force generated by the comb drives to the nanofiber itself rather than to the supporting tethers. The net-force output by the actuator in a tension experiment is calculated as the difference between the electrostatic actuation and the lateral force consumed by the tethers according to (3). Uncertainties in the measurement of each of these forces increase the uncertainty in the net axial force applied to the fiber specimen. Furthermore, since the force stored in the tethers is commonly calculated by measuring their lateral deflection multiplied by their stiffness, the accuracy in the determination of the net output force depends on the accuracy in the measurement of the tether deflection. Hence, reducing the tether stiffness improves the accuracy in determining the net output force and, therefore, the nanofiber properties. It is to be noted that it is assumed that the tethers' stiffness is accurately measurable by the method explained in Section III-B. Therefore, it does not affect the uncertainty in the force measurement.

Thus, on the one hand, it is desirable to incorporate compliant tethers to improve the accuracy in the tether force measurement, but on the other hand, compliant tethers result in small restoring force and small maximum force output by the comb drive due to the reduced pull-in voltage. Because of these considerations, an optimum design is sought for feasible and accurate nanofiber testing. In order to quantify the effect of tether stiffness on the uncertainty in the force output, the comb-drive force efficiency

$eff$  was defined as a dimensionless measure of the relative difference between the electrostatic force and the lateral force absorbed by the tethers

$$eff = \frac{F_{net}}{F_E} = \frac{(Nh\epsilon_0 V^2/g - n_t P(\delta))}{Nh\epsilon_0 V^2/g}. \quad (13)$$

The importance of this quantity and its relevance to our device design can be understood by the fact that the force efficiency, as defined in (13), is a measure of the relative uncertainty in the force applied to a nanofiber by a comb-driven mechanical testing device. To show the relevance between the two, first, we define the operator  $\Delta_\lambda(\cdot)$  as the uncertainty in a calculated quantity, such as fiber force ( $\cdot$ ), caused by an uncertainty  $\lambda$  in the measurement of the fiber elongation  $\delta$ , which is the same as the tether deflection. Since the electrostatic force is calculated from the applied voltage independently of the fiber elongation  $\delta$ , then  $\Delta_\lambda(F_E) = 0$ . Therefore, the uncertainty in calculating the fiber force is

$$F_{net} = F_E - F_t \Rightarrow \Delta_\lambda(F_{net}) = \Delta_\lambda(F_E) - \Delta_\lambda(F_t) = -\Delta_\lambda(F_t). \quad (14)$$

According to (14), the uncertainty in the lateral tether deflection is required to calculate the uncertainty in the fiber force. Since the force consumed by the tethers,  $F_t$ , is only a function of the tethers' deflection, the measurement of this force is accurate within the uncertainty  $\Delta_\lambda(F_t) \approx (dF_t/d\delta)\lambda$ . Based on (13),  $F_t$  can be expressed in terms of the comb-drive force efficiency and the force in the fiber as  $F_T = F_{net}(1/eff - 1)$ . Therefore, (14) can be rewritten as

$$\Delta_\lambda(F_{net}) = \Delta_\lambda(F_T) \approx \frac{dF_{net}}{d\delta} \left( \frac{1}{eff} - 1 \right) \lambda - F_{net} \left( \frac{1}{eff^2} \frac{deff}{d\delta} \right) \lambda. \quad (15)$$

We have safely assumed that the force in the fiber is constant when the fiber undergoes plasticity, i.e.,  $dF_{net}/d\delta = 0$ , and (15) can be simplified to give the relative uncertainty in the calculated value for the force applied to the fiber as

$$\frac{\Delta_\lambda(F_{net})}{F_{net}} \approx \left( \frac{1}{eff^2} \frac{deff}{d\delta} \right) \lambda \quad (16)$$

which is described in terms of the comb-drive force efficiency and its change during an experiment. Therefore, a higher comb-drive force efficiency results in higher relative accuracy in the calculation of the force applied on the fiber. Hence, the second objective of our design procedure is achieved by maximizing the force efficiency within the design constraints in Table I.

Clearly, the force efficiency is a function of the mechanical behavior of the nanofibers, which helps us to design actuators suited to test nanofibers with properties in a particular range of values. For polymer fibers with elastic–perfectly plastic mechanical behavior, the force efficiency is the largest in the regime of elastic-fiber deformation, while it decreases

as the fiber deforms plastically (becoming more compliant) since the net output force is constant while voltage is still increasing to further deflect the tethers and also extend the nanofiber.

In addition to these two design considerations, the device dimensions are also limited by constraints related to the fabrication process (photolithographic patterning) and by device reliability concerns, such as deviation from planarity due to component self-weight and adhesion to the substrate (stiction). In this design process, the number of comb fingers in each device was limited to 200 to prevent release and operation surface adhesion (stiction) and to enhance the fabrication yield. It is to be noted that a comb drive with 200 comb fingers is a freestanding structure that is 1 mm long. Larger structures have been shown to have reliability issues [33]. A large number of comb fingers may limit the yield of useful devices because small debris under a comb finger often render the comb drive inoperable. Finally, the optimization parameters were the tether length  $l$  and width  $w$ , as shown in Table II.

During the design optimization, for each value of the tether width  $w$ , and number of pairs of comb fingers  $N$ , the tether length  $l$  was calculated as a function of the pull-in voltage by (10) and (11). The set of quantities  $N$ ,  $w$ , and  $l$ , along with the dimensions in Table I, was determined for a single comb-drive array. Next, the maximum net output force was calculated from (2) and (3), and the device designs that did not output sufficient force to plastically deform a fiber, according to Table I, were eliminated. In the next step, the force efficiency for each device as a function of nanofiber extension was obtained by (13). An example of the force efficiency versus the fiber extension is shown in Fig. 5, which points to a steady decline in the force efficiency with fiber extension (and actuator motion) after fiber yielding. At large fiber extensions (actuator motions), the device efficiency drops steadily [see later the error bars in Fig. 9(b)]. The device force efficiency at the largest fiber extension as a function of pull-in voltage is shown in Fig. 6. Each point represents a set of values for  $N$ ,  $w$ , and  $l$ , which, together with the geometrical constants in Table I, are sufficient to design a comb drive. A sample calculation is shown in the Appendix. The constraint for the tether length ( $l < 500 \mu\text{m}$ ) is shown with a solid line. Among all devices with the same width, the device force efficiency decreases as the pull-in voltage increases due to the increased tether stiffness required to prevent the pull-in instability. Similarly, at constant tether length, increasing tether width results in increased pull-in voltage, which, in turn, decreases the device force efficiency. Therefore, slender tethers help to achieve high device force efficiency (second objective), provided that they allow for sufficient force to deform a fiber plastically (first objective). The most effective geometric parameter in increasing the force efficiency, as observed in Fig. 6, is the length of the tethers, which is only limited by fabrication constraints.

Given the geometry constraints in Table II, the optimal devices with 100 pairs of fingers are encircled in Fig. 6. For other choices of  $N$ , e.g., 40 and 200, the same procedure was followed for force efficient devices to test slender or thicker nanofibers. Therefore, the resulting devices had more than 90% force efficiency in the elastic regime of fiber deformation,

TABLE II  
DESIGN VARIABLES FOR A COMB-DRIVE ACTUATOR

Design	Value range ( $\mu\text{m}$ )	Comments
Width of tethers ( $w$ )	1.8 – 3.0	Minimum value is limited by fabrication, maximum value is limited by large stiffness of the resulting tethers
Length of tethers ( $l$ )	< 500	Maximum value is limited by beam bending at its tip due to self load and adhesion (stiction) upon HF release from the sacrificial layer. The main concern comes from the tethers supporting the long moving comb-finger array.
Number of comb-fingers ( $N$ )	40, 100, 200	40 for smallest fibers: strength < 5 $\mu\text{N}$ 100 for fiber strength 5 $\mu\text{N}$ - 25 $\mu\text{N}$ 200 for fiber strength >25 $\mu\text{N}$

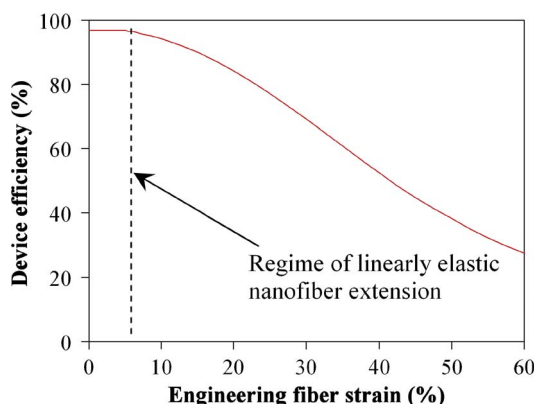


Fig. 5. Device force efficiency as a function of fiber strain calculated from (11) for  $N = 100$ . The pull-in voltage is 220 V, and the tether-beam width and length are 1.8 and 300  $\mu\text{m}$ , respectively.

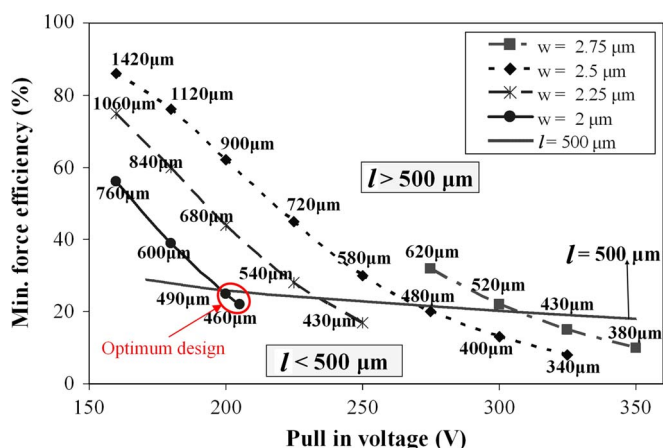


Fig. 6. Minimum force efficiency at 10  $\mu\text{m}$  of fiber extension (device translation) and for output force of 25  $\mu\text{N}$ , as calculated from (13). Calculations were conducted for 100 pairs of comb fingers and three pairs of tethers, as shown in Fig. 1. The numbers along the curves indicate the tether lengths.

which dropped to about 20% at 50% engineering strain. The high force efficiency in the regime of elastic-fiber extension is absolutely critical in computing the elastic modulus of the

nanofibers since this calculation includes small values of force at the beginning of fiber loading.

### III. APPLICATION TO POLYMERIC NANOFIBERS

#### A. Fabrication of Test Platform and Nanofiber Preparation

MEMS devices were fabricated at Case Western Reserve University, Cleveland, OH, by surface micromachining following our design considerations presented in the previous section. They consisted of a 6- $\mu\text{m}$  structural layer of polysilicon on top of thermally grown silicon dioxide that served as insulator. To increase the conductivity of the devices for electrostatic actuation, they were sputter-coated with a 20-nm layer of Au-Pt. On average, each device occupied 1  $\text{mm}^2$  on a die, most of which were the large anchoring pads that ensured connection to the substrate after timed etching. The test samples were PAN nanofibers electrospun from a solution of PAN in dimethyl formamide. The resulting nanofibers had uniform diameter along their length, and their surfaces were smooth so that there were no discernible surface features upon inspection by an SEM.

#### B. Calibration of the Tether Stiffness

The relationship between the lateral force in the tethers of a comb-drive actuator and their deflection is required to quantify the net output force to a nanofiber. While this relationship can be calculated by measuring the dimensions of the device with an SEM, uneven tether width and uncertainties in the boundary conditions result in major deviations from the calculated stiffness. Therefore, the tether stiffness was determined experimentally. A procedure that is based on macroscale practices was applied, which provided a traceable force calibration of the device tethers' stiffness. The first step in this method involved the calibration of an auxiliary MEMS-scale folded-beam load cell, which, in turn, was used to measure the stiffness of the comb-drive tethers.

In the first step, glass beads from Corpuscular Inc. with known density were attached with an epoxy adhesive to the tip

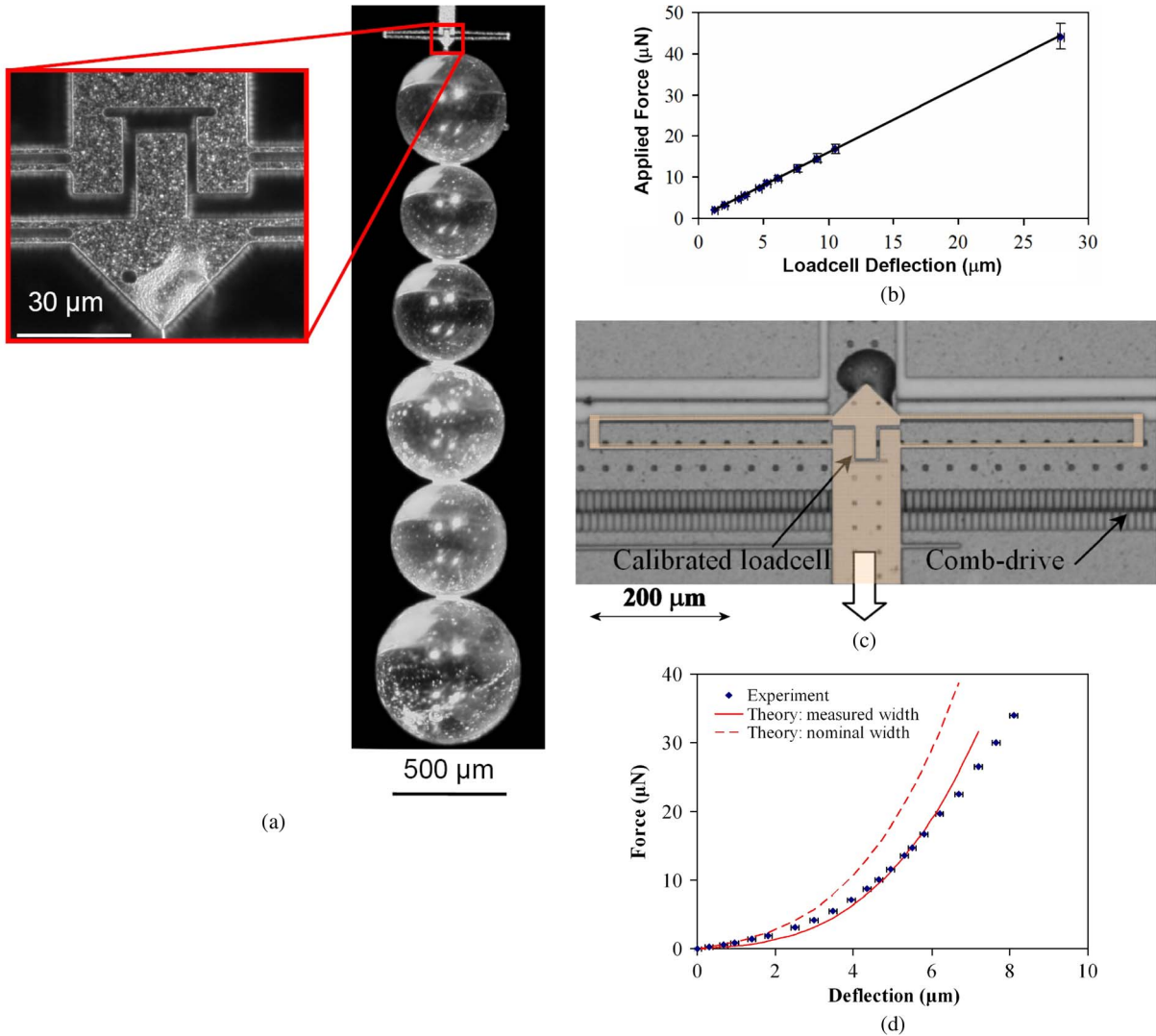


Fig. 7. (a) Micromachined folded-beam load cell calibrated by attaching microscale beads of known density at its tip. (b) Force–deflection curve for the folded-beam load cell in (a). (c) Precalibrated load cell is attached to a comb drive to calibrate the bending stiffness of the comb-drive tethers. In this image, the calibrated load cell was artificially colored to distinguish it from the comb drive that is underneath it. (d) Force-versus-deflection curve of the tethers of a comb-drive actuator, as measured experimentally and computed by using the nominal and measured widths of the tethers.

of a vertically mounted surface-micromachined folded-beam load cell, as shown in Fig. 7(a). The thin adhesive layer was significantly smaller than the diameters of the glass beads. Therefore, the adhesive did not contribute to the total weight by any significant measure. The stiffness of this auxiliary load cell was calculated as a curve of its deflection versus the cumulative weight of the beads, as seen in Fig. 7(b). The load-cell extension in the inset of Fig. 7(a) was calculated by digital image correlation (DIC) with an accuracy of one-tenth of an image pixel, as described in [12] and [13], with each pixel being  $\sim 200$  nm. This method has been developed by the authors to provide the ability for high-resolution experiments in the ambient environment without the need to expose the sensitive polymeric nanofibers to an electron beam. Then, the load cell's stiffness was computed by multiplying the density of the beads by their dimensions, which were measured optically. The calibration curve in Fig. 7(b) shows that the deflection of the load cell was linear with respect to the applied force until quite-large deflections. The uncertainty in this method,

estimated to be about 3%, mostly stems from the inaccuracy in the measurement of the beads' diameters. Compared to other traceable calibration methods [34], the present method provides a linear calibration curve until large load-cell deflections and has significantly higher accuracy because of the subpixel resolution of the DIC method that is applied to calculate the load-cell opening deflection.

In the second step, the precalibrated load cell was attached onto a comb drive by using an external probe and an alignment system to deflect the comb drive in its natural loading direction, as shown in Fig. 7(c). The deflections of the tethers and the load cell were then computed by DIC from optical images with resolution of 25 nm or better [12], [13]. Combined with the experimentally measured stiffness of the load cell, the lateral force on the tethers as a function of their deflection was then computed. An example of a calibration curve for the tether stiffness is shown in Fig. 7(d). The experimental calibration curves matched relatively well with the theoretical curves obtained from (4) and (5) by considering the dimensions of the

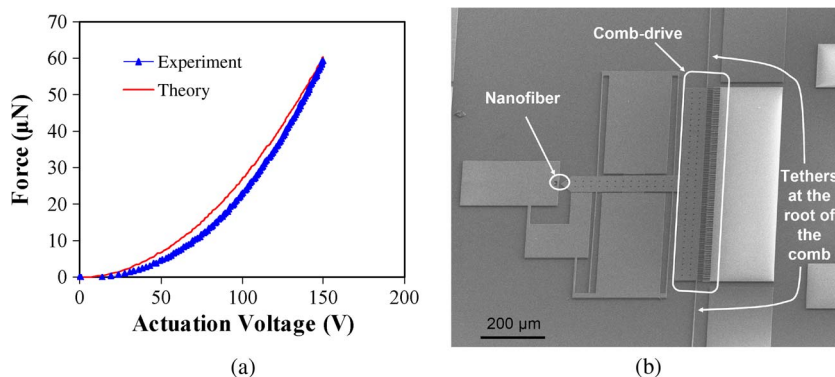


Fig. 8. (a) Electrostatic force generated by the comb drive in (b) as a function of actuation voltage.

tethers, as measured with an SEM. For comparison purposes, the theoretical and experimental force–deflection curves of the tethers are shown in Fig. 7(d). A possible source for the difference between the experimental and the calculated deflection of the tethers using the measured tether dimensions may be the assumption for no rotation at the two ends of the “fixed–fixed” tether beam. At large beam deflections, the high force may lead to material deformation at the support that distorts the originally  $90^\circ$  angle between the beam and its support. A finite-element analysis would be able to capture the effect of the support compliance, but such results are strongly affected by the precise details of this support that are not always known. Therefore, in this paper, we always employed the experimental force–deflection curves for the tethers that take into account the effect of compliant supports.

### C. Measurement of the Mechanical Behavior of Polymeric Nanofibers

The fabricated MEMS devices were used to investigate the mechanical behavior of PAN nanofibers with expected fiber strength of up to  $25 \mu\text{N}$  and large extensional strains. For the particular needs in force output, devices with 100 pairs of comb fingers were chosen. First, the electrostatic force as a function of actuation voltage was measured for each device prior to mounting a fiber. In principle, this force could be calculated directly from (2), given the actuation voltage. However, in practice, due to imperfections in the geometry of the devices and variations of the electric field at the finger boundaries [35], an experimental calibration is required. To measure the electrostatic force as a function of actuation voltage, a voltage ramp of 0–200 V was applied in 120 s, and the displacement of the moving set of fingers was calculated as a function of voltage by DIC. Combining this curve with the force-versus-deflection curves of the tethers shown in Fig. 7(d), the electrostatic force was calculated as a function of voltage. An example is shown in Fig. 8(a). This curve can be fitted well to (2) as  $F(\mu\text{N}) = 0.0023 V^2$  (in volts). The theoretical coefficient of proportionality between the force and square of voltage calculated from (2) was  $0.0026 \mu\text{N}/\text{V}^2$ , which was 12% higher than the experimental value, possibly due to imperfections in the dimensions of the device. These theoretical and experimental curves of the electrostatic force versus the actuation voltage are shown in Fig. 8(a).

Individual PAN nanofibers were then mounted on the device [see Fig. 8(b)] by the method explained in [12]. A voltage ramp was applied to the device, and the extension of the sample, which is equal to the motion of the moving comb, and the lateral deflection of the tethers were computed by DIC. Next, the force applied to the tethers as a function of voltage was calculated by measuring the tethers’ deflection and by using their stiffness calibration curves obtained in Section III-B. The axial force in the fiber was the difference between the electrostatic force and the tether force. The engineering stress in the fiber was calculated by dividing the fiber axial force by the initial fiber cross section, which was measured by postmortem SEM from undeformed segments of the tested nanofibers, and the engineering strain was computed by dividing the fiber extension by its initial length, which was measured by optical microscopy. An example of the force exerted on a tether as a function of the applied voltage, with and without a fiber, and the associated engineering-stress-versus-strain curve are shown in Fig. 9(a) and (b), respectively. The error bars in Fig. 9(b) indicate that the uncertainty in force measurement increases as the fiber extension increases (in other words, as the device force efficiency decreases according to the previous discussion). Following the same methodology, repeated loading–unloading curves were also obtained, and an example is shown in Fig. 9(c) and (d). Finally, Fig. 9(e) shows an SEM image of a polymer nanofiber after being drawn by the comb-drive actuator and the applied voltage was removed. In all tests, the fibers extended to  $\sim 50\%$  strain, but they did not rupture, remaining on the chip for postmortem imaging. A summary of the measured mechanical properties of the electrospun PAN nanofibers tested with this method is presented in Table III. The measurements of yield strength and elastic modulus were quite consistent with two outlier points in each case, which may be stemming from variations in properties between fibers as a function of their diameter or local defects that initiate early yielding. Yielding of the nanofibers tested here occurred as described in previous publications by this group [12], [13], where multiple surface ripples formed along the entire length of each nanofiber. This mode of deformation is not the only one for PAN nanofibers, and it occurs only for certain electrospinning conditions. The mechanical strength, on the other hand, which is only a conservative value at, on average, 50% engineering strain (the fibers were not tested to ultimate failure), was quite

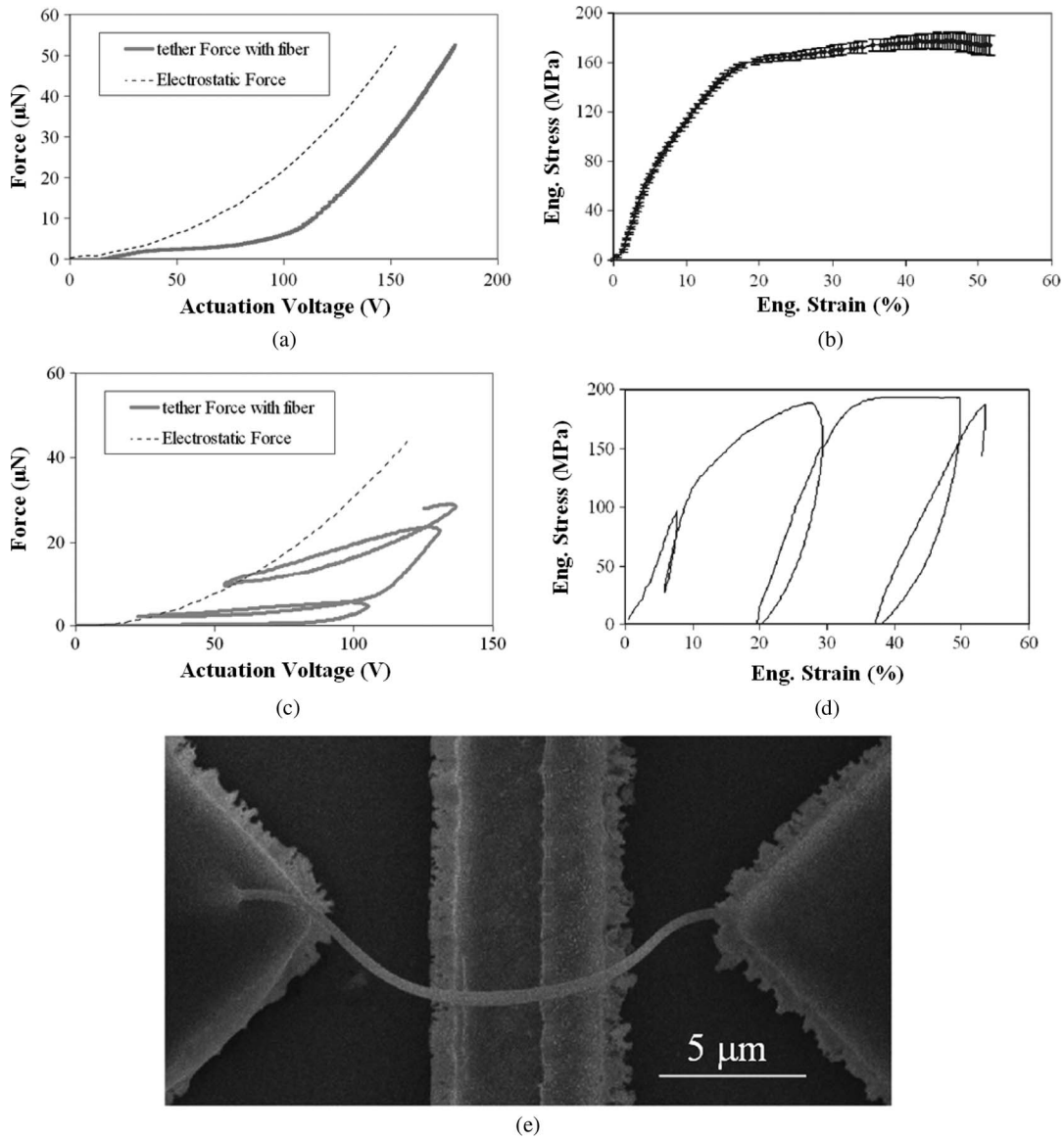


Fig. 9. (a) Electrostatic force and force stored in the tethers in the presence of a specimen as a function of applied voltage during monotonic loading. (b) Stress–strain curve for a PAN nanofiber [uncertainty bars are included, showing an increase at large fiber extensions (see the text)]. (c) Electrostatic force and force stored in the tethers in the presence of a specimen as a function of applied voltage during repeated loading–unloading. (d) Stress–strain curve during repeated loading–unloading. (e) SEM image of a PAN fiber plastically extended by electrostatic loading.

TABLE III  
 MECHANICAL PROPERTIES OF PAN NANOFIBERS MEASURED WITH THE MEMS PLATFORM IN FIG. 8(b)

Test Number	E (GPa)	$\sigma_{\text{yield}}$ (MPa)	$\sigma_{\text{strength}}^*$ (MPa)	$\epsilon_f^*$ (%)
1	2.1	167	190	61
2	4.4	108	171	50
3	3.1	100	206	60
4	1.8	81	177	55
5	3	91	192	53
6	3.9	183	224	58
7	2.9	143	156	44
<b>Average</b>	<b>3.0±0.9</b>	<b>125±39</b>	<b>188±22</b>	<b>56</b>

\* Samples were stretched plastically but they did not fail

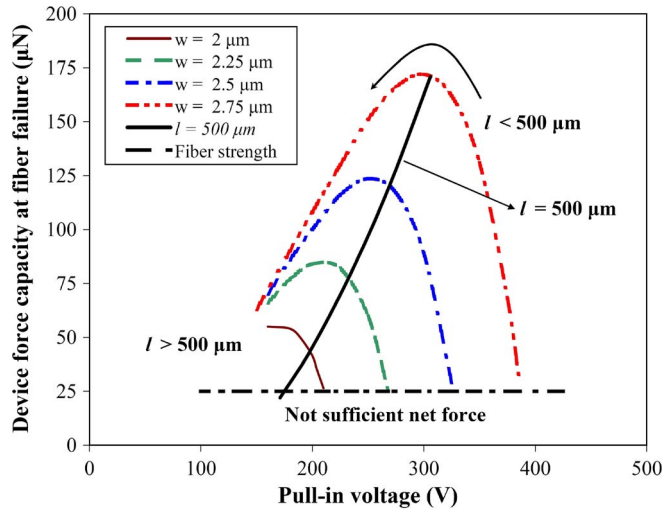


Fig. 10. Net output force of comb drives with different dimensions at 10- $\mu\text{m}$  actuation, as calculated from (2). All devices had  $N = 100$  pairs of fingers and three pairs of tethers. Each curve represents a specific tether width. The length of the tethers increases in the direction of the arrow at the top of the plot.

consistent, and it scaled with the value of the strain at which it was recorded. A comparison of these measurements with data obtained by an independent method will be presented in the next section.

#### IV. DISCUSSION

Although the electrostatic force depends on the pairs of comb fingers  $N$ , in (1), higher net-force output to a fiber is not achieved by simply increasing  $N$ . This is an incorrect practice in designing MEMS platforms for mechanical testing of nanostructures without properly accounting for the limiting pull-in voltage and its consequences to device design. Increasing  $N$ , while all other geometry parameters are held constant, results in reduction of the pull-in voltage, according to (12b). Hence,  $NV_{\text{pull-in}}^2$  in (3) should be considered as one term in order to calculate the desired force on a fiber, while  $N$ , according to (12b), is a parameter to limit the maximum pull-in voltage, at the expense of constructing larger comb drives, so that dielectric breakdown does not occur prematurely.

On the other hand, increasing the pull-in voltage by incorporating stiffer tethers, as a means to increase the net output force, is only effective for small nanofiber extensions and actuator motions, where the share of the tethers in the force generated by the comb drives is small. In large fiber extensions, however, stiffer tethers significantly reduce the net output force. Even more adversely, stiffer tethers result in the reduction of the force efficiency of the device, and consequently, they reduce the accuracy in force measurements. It is therefore advisable that slender tethers be incorporated to the extent that is possible so that sufficient force can be generated onto a nanofiber.

With respect to the effect of tether stiffness on the net output force, Fig. 10 shows two regimes that are separated by the solid line for  $l = 500 \mu\text{m}$ . The family of curves in Fig. 10 is calculated at an instant of a tension test at which the nanofiber was extended by  $10 \mu\text{m}$ , i.e., the comb drive had moved by  $10 \mu\text{m}$ . The curves would shift downward if the

actuator motion increased further, but the general trend would remain the same. In the first regime ( $l > 500 \mu\text{m}$ ), the tether force,  $P(\delta)$  in (2), is negligible throughout the experiment due to either high compliance of the tethers or small actuator motions. Thus, the output force increases monotonically with the pull-in voltage. This is a common regime of operation of comb drives. In the second regime ( $l < 500 \mu\text{m}$ ), a decline in the comb drive's net output force as a function of pull-in voltage occurs at high pull-in voltages. High pull-in voltages require stiffer tethers that, in turn, absorb a larger portion of the electrostatic force and thus reduce the net output force. Therefore, the distinction between the two regimes is owed to the compliance of the tethers and the amount of force that they absorb at high deflections ( $10 \mu\text{m}$  in this case) relative to the total electrostatic force generated by the actuator. The second regime of operation was used in this investigation in order to meet the requirement for large nanofiber extensions by using short beams ( $l < 500 \mu\text{m}$ ). Finally, according to Fig. 10, in order to test nanofibers that are substantially stiffer, one may need to use wider tethers, i.e.,  $w \geq 2.25 \mu\text{m}$ , to increase the force capacity of the comb drives. The maximum length of  $500 \mu\text{m}$  was imposed to maintain the reliability of these slender structures during sacrificial release from their substrate by wet processing. One may obtain more efficient devices by using longer tethers. For example, according to Fig. 6, significantly higher device force efficiencies of up to 60% could have been achieved by incorporating tethers that are  $760 \mu\text{m}$  long and  $2 \mu\text{m}$  wide. However, such tethers are very fragile and would have resulted in very low fabrication yield.

An additional constraint was the device height (thickness) that was set to be  $6 \mu\text{m}$ , as this was determined by the fabrication process that was employed. The effect of device height  $h$  may be assessed by combining (13) with (3) as

$$eff = \frac{\text{net force on fiber}}{\text{total force}} = \frac{F_{\text{net}}}{F_{\text{net}} + n_t P(\delta)}. \quad (17)$$

When all geometrical parameters and the mechanical behavior of the fiber remain the same, an increase in the device thickness increases the tether stiffness and thus reduces the device force efficiency. In other words, thicker devices are appropriate only if the fiber stiffness increases; otherwise, the device efficiency will be reduced. Therefore, the device design considerations discussed in this paper are also applicable to thicker devices fabricated by deep RIE (DRIE) or lithographic galvanoformung abformung, which achieve high-aspect-ratio comb drives, so that stiffer microfibers can be tested.

In order to assess the accuracy of this mechanical testing platform in measuring the mechanical behavior of ductile nanofibers, we compared the mechanical properties in Table III acquired at an average strain rate of  $0.0032 \text{ s}^{-1}$  with those obtained by a method developed by the authors in the past [12], [13] using external actuation at a similar strain rate of  $0.0025 \text{ s}^{-1}$ . Note, however, that the device presented here does not provide a constant strain rate throughout an experiment. This is because the force output by the comb drive is unevenly distributed between the tethers and the nanofiber over the course of time. Even at the plateau of force in Fig. 9(b), the

TABLE IV  
MECHANICAL PROPERTIES OF PAN NANOFIBERS MEASURED BY AN  
OFF-CHIP ACTUATED MEMS PLATFORM FOR NANOFIBER TESTING [12],  
[13]. DATA WERE OBTAINED AT  $0.0025\text{-s}^{-1}$  STRAIN RATE

Test Number	E (GPa)	$\sigma_{\text{yield}}$ (MPa)	$\sigma_{\text{strength}}$ (MPa)
1	3.3	86	127
2	4.0	71	165
3	3.4	107	150
4	3.5	130	157
<b>Average</b>	$3.6\pm 0.3$	$98\pm 26$	$150\pm 16$

strain rate in the fiber is still not constant. The aforementioned deficiencies are actually common among all MEMS devices that incorporate supporting tethers. The average values of the mechanical properties in Tables III and IV obtained by the two methods are in good agreement, particularly in terms of elastic moduli. On the other hand, the strength and yield stress measured by the present devices were higher on average. This difference in the values of fiber strength and yield stress could stem from the variable strain rate that has been shown to have an effect on the mechanical behavior of polymeric nanofibers [13] and the size effect associated with the nanofiber diameter.

## V. CONCLUSION

MEMS-based tensile testing platforms with comb-drive actuators were designed for optimal performance as mechanical characterization tools for ductile polymeric nanofibers. Based on the actuation distance of the comb drives, the following two regimes of operation were distinguished: 1) For small fiber extensions, the actuator net output force was shown to increase with tether stiffness which increased the voltage at the pull-in instability, while 2) for large fiber extensions, which were of interest in this paper, compliant tethers were more desirable since they provided better accuracy in sample force measurement and higher net output force. Incorporating compliant tethers has two opposing effects on the net output force: 1) It reduces the maximum total force of the comb drives by a reduction in the pull-in voltage, and 2) it reduces the share of the tethers in the total force. In sufficiently large fiber extensions and for compliant tethers, the reduction in the total force is outweighed by the reduction in the tether force, so more compliant tethers increase the maximum force output to the nanofiber.

In order to provide sufficient force to extend the nanofibers plastically prior to the device pull-in instability and, at the same time, to increase the accuracy in measuring the net device output force, an optimization metric was applied, namely, the comb-drive force efficiency, which accounts for the effect of the nanofiber stiffness on the net electrostatic force. Maximizing this metric results in the design of comb-drive actuators for nanoscale tensile testing platforms in which polymeric nanofibers with elastic–perfectly plastic mechanical behavior could be tested with reduced relative uncertainty in the calculation of the applied force. This uncertainty was minimal

in the elastic regime, but it increased after fiber yielding. The mechanical behavior of PAN nanofibers measured with this device was comparable with that obtained before with the aid of off-chip actuators. Specifically, the elastic modulus and the tensile strength of the particular PAN nanofibers were in the ranges of 2–4 GPa and 140–200 MPa, respectively.

The results of this paper point to the potential in using comb-drive actuators in load-controlled MEMS tension testing platforms for nanoscale experimentation with ductile samples that require deformations that are larger than a couple of micrometers [11], [20]. Such experiments can be optimized so that the uncertainty in the calculation of the force on the sample is small: Unlike conventional mechanical testing tools, which can be used for a wide range of sample stiffnesses, comb drives are most effective only when they are designed for specific samples.

## APPENDIX

An example of the design of a comb-drive actuator, which was discussed in Section II-B, is presented here. We consider a device that is required to output a fiber drawing force of  $25\ \mu\text{N}$  at a tether deflection/sample extension of  $\delta = 10\ \mu\text{m}$ . Based on the constraints in Tables I and II, the number of comb fingers for the desired force is  $N = 100$ . In addition, we assume that  $\xi_i = 0.05$ ,  $g = 100\ \text{nm}$ ,  $g = 2\ \mu\text{m}$ ,  $h = 6\ \mu\text{m}$ , and  $l_i = 3\ \text{g}$ .

The calculation of the dimensions of the tethers begins with the input values for  $V_{\text{pull-in}}$  and the width of the tethers,  $w$ , which correspond to a datum point in Figs. 6 and 10. The same calculation is then carried out for other values of  $w$  and  $V_{\text{pull-in}}$  within the constraints in Tables I and II, and the device with the highest force efficiency, among those generating sufficient force to the sample (see Tables I and II), is selected.

A device with  $w = 2\ \mu\text{m}$  demonstrates lateral instability at  $V_{\text{pull-in}} = 200\ \text{V}$ . Therefore, the values of all the parameters in (10) and (11) are known, except for  $\xi_{\text{ins}}$  and  $l$ . These equations are then solved, giving  $\xi_{\text{ins}} = 0.195$  and  $l = 489\ \mu\text{m}$ . The maximum electrostatic force generated by the comb drive is calculated using (3) at the pull-in voltage

$$F = \frac{N h \epsilon_0 V_{\text{pull-in}}^2}{g} = 116\ \mu\text{N}. \quad (\text{A.1})$$

Part of this force is balanced by the spring force in the tethers, which is calculated from (4) and (5) for the desired deflection by considering the known tether geometry (specified by the selected width of  $2\ \mu\text{m}$  and the calculated length of  $489\ \mu\text{m}$ ), which is equal to  $74.2\ \mu\text{N}$ .

Therefore, the maximum force that can be applied on a fiber is calculated from (3) to be  $41.5\ \mu\text{N}$ , which is more than the required force of  $25\ \mu\text{N}$ . Thus, the device can provide sufficient force to extend the nanofiber. A force in excess of  $25\ \mu\text{N}$  does not violate the axial force equilibrium in the device; it simply implies that the fiber will be stretched to  $\delta = 10\ \mu\text{m}$  at voltages that are less than the pull-in voltage. In this case, the maximum voltage required to deform the nanofiber to the desired length can be estimated by setting the net force in (3) equal to  $25\ \mu\text{N}$ , which results in  $185\ \text{V}$ . Therefore, the fiber is fully stretched when a voltage of  $185\ \text{V}$  is applied. The electrostatic force at

this voltage is calculated from (3) to be  $98 \mu\text{N}$ , and the comb-drive force efficiency can be calculated from (13) as

$$eff = \frac{(Nh\epsilon_0 V^2/g - n_t P(\delta))}{Nh\epsilon_0 V^2/g} = \frac{25}{98} \approx 26\%. \quad (\text{A.2})$$

#### ACKNOWLEDGMENT

The authors would like to thank Prof. H. Kahn from Case Western Reserve University for fabricating the MEMS devices and Dr. V. Petrova for her assistance in SEM imaging of the nanofibers.

#### REFERENCES

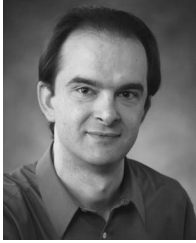
- [1] R. S. Barhate, C. K. Loong, and S. Ramakrishna, "Preparation and characterization of nanofibrous filtering media," *J. Membr. Sci.*, vol. 283, no. 1/2, pp. 209–218, Oct. 2006.
- [2] Y. Zhao, J. Jin, and X. Yang, "Hydrothermal synthesis of titanate nanowires arrays," *Mater. Lett.*, vol. 61, no. 2, pp. 384–388, Jan. 2007.
- [3] T. Ondarcuhu and C. Joachim, "Drawing a single nanofiber over hundreds of microns," *Europhys. Lett.*, vol. 42, no. 2, pp. 215–220, Apr. 1998.
- [4] B. B. Lakshmi, C. J. Patrissi, and C. R. Martin, "Sol-gel template synthesis of semiconductor oxide micro- and nanostructures," *J. Chem. Mater.*, vol. 9, no. 11, pp. 2544–2550, Nov. 1997.
- [5] Z. M. Huang, Y. Z. Zhang, M. Kotaki, and S. Ramakrishna, "A review on polymer nanofibers by electrospinning and their applications in nanocomposites," *Compos. Sci. Technol.*, vol. 63, no. 15, pp. 2223–2253, Nov. 2003.
- [6] F. Ko, Y. Gogotsi, A. Ashraf, N. Naguib, H. Ye, G. Yang, C. Li, and P. Willis, "Electrospinning of continuous carbon nanotube-filled nanofiber yarns," *Adv. Mater.*, vol. 15, no. 14, pp. 1161–1165, Jul. 2003.
- [7] S. Cuenot, S. Demoustier-Champagne, and B. Nysten, "Elastic modulus of polypyrrole nanotubes," *Phys. Rev. Lett.*, vol. 85, no. 8, pp. 1690–1693, Aug. 2000.
- [8] E. Zussman, X. Chen, W. Ding, L. Calabri, D. A. Dikin, J. P. Quintana, and R. S. Ruoff, "Mechanical and structural characterization of electrospun PAN-derived carbon nanofibers," *Carbon*, vol. 43, no. 10, pp. 2175–2185, Aug. 2005.
- [9] S. Lu, Z. Guo, W. Ding, and R. S. Ruoff, "Analysis of a microelectromechanical system testing stage for tensile loading of nanostructures," *Rev. Sci. Instrum.*, vol. 77, no. 5, p. 056103(1–4), May 2006.
- [10] Y. Zhu, N. Moldovan, and H. D. Espinosa, "A microelectromechanical load sensor for *in situ* electron and X-ray microscopy tensile testing of nanostructures," *Appl. Phys. Lett.*, vol. 86, no. 1, p. 013506(1–3), Jan. 2005.
- [11] M. Kiuchi, Y. Isono, S. Sugiyama, T. Morita, and S. Matsui, "Mechanical and electrical properties evaluation of carbon nanowire using electrostatic actuated nano tensile testing devices (EANAT)," in *Proc. 5th IEEE Conf. Nanotechnol.*, Nagoya, Japan, 2005, pp. 486–489.
- [12] M. Naraghi, I. Chasiotis, Y. Dzenis, Y. Wen, and H. Kahn, "Novel method for mechanical characterization of polymeric nanofibers," *Rev. Sci. Instrum.*, vol. 78, no. 8, p. 085108(1–7), Aug. 2007.
- [13] M. Naraghi, I. Chasiotis, Y. Dzenis, Y. Wen, and H. Kahn, "Mechanical deformation and failure of electrospun polyacrylonitrile nanofibers as a function of strain rate," *Appl. Phys. Lett.*, vol. 91, no. 15, p. 151901(1–3), Oct. 2007.
- [14] M. M. Tillemann, "Analysis of electrostatic comb-driven actuators in linear and nonlinear regions," *Int. J. Solids Struct.*, vol. 41, no. 18/19, pp. 4889–4898, Sep. 2004.
- [15] T. Akiyama, D. Collard, and H. Fujita, "Scratch drive actuator with mechanical links for self-assembly of three-dimensional MEMS," *J. Microelectromech. Syst.*, vol. 6, no. 1, pp. 10–17, Mar. 1997.
- [16] M. P. De Boer, D. L. Luck, W. R. Ashurst, R. Maboudian, A. D. Corwin, J. A. Walraven, and J. M. Redmond, "High-performance surface micro-machined inchworm actuator," *J. Microelectromech. Syst.*, vol. 13, no. 1, pp. 63–74, Feb. 2004.
- [17] S. J. Eppell, B. N. Smith, H. Kahn, and R. Ballarini, "Nano-measurements with micro-devices: Mechanical properties of hydrated collagen fibrils," *J. R. Soc. Interface*, vol. 3, no. 6, pp. 117–121, Feb. 2006.
- [18] Q. A. Huang and N. K. Shek Lee, "Analysis and design of polysilicon thermal flexure actuator," *J. Micromech. Microeng.*, vol. 9, no. 1, pp. 64–70, Mar. 1999.
- [19] Y. Zhu, A. Corigliano, and H. D. Espinosa, "A thermal actuator for nanoscale *in situ* microscopy testing: Design and characterization," *J. Micromech. Microeng.*, vol. 16, no. 2, pp. 242–253, Feb. 2006.
- [20] M. A. Haque and M. T. Saif, "Microscale materials testing using MEMS actuators," *J. Microelectromech. Syst.*, vol. 10, no. 1, pp. 146–152, Mar. 2001.
- [21] R. Legtenberg, A. W. Groeneveld, and M. Elwenspoek, "Comb-drive actuators for large displacements," *J. Micromech. Microeng.*, vol. 6, no. 3, pp. 320–329, Sep. 1996.
- [22] C. Chen and C. Lee, "Design and modeling for comb-drive actuator with large static displacement," *Sens. Actuators A, Phys.*, vol. 115, no. 2/3, pp. 530–539, Sep. 2004.
- [23] J. D. Grade, H. Jerman, and T. W. Kenny, "Design of large deflection electrostatic actuators," *J. Microelectromech. Syst.*, vol. 12, no. 3, pp. 335–343, Jun. 2003.
- [24] R. Frisch-Fay, *Flexible Bars*. London, U.K.: Butterworth, 1962, pp. 83–90.
- [25] I. Chasiotis, "Mechanics of thin films and microdevices," *IEEE Trans. Device Mater. Rel.*, vol. 4, no. 2, pp. 176–188, Jun. 2004.
- [26] J. Yang, H. Kahn, A. Q. He, S. M. Phillips, and A. H. Heuer, "A new technique for producing large-area as-deposited zero-stress LPCVD polysilicon films: The MultiPoly process," *J. Microelectromech. Syst.*, vol. 9, no. 4, pp. 485–494, Dec. 2000.
- [27] Y. S. Liao, S. W. Chyuan, and J. T. Chen, "Numerical studies of variations in the gap and finger width ratio and travelled distance for the driving force of a radio-frequency microelectromechanical system device using the dual boundary element method," *Proc. Inst. Mech. Eng. C, Mech. Eng. Sci.*, vol. 218, pp. 1243–1253, 2004.
- [28] V. P. Jaecklin, C. Linder, N. F. de Rooij, J. M. Moret, R. Bischof, and F. Rudolf, "Novel polysilicon comb actuators for xy-stages," in *Proc. IEEE Micro Electro Mech. Syst.*, 1992, pp. 147–149.
- [29] M. J. Madou, *Fundamentals of Micromachining*, 2nd ed. Boca Raton, FL: CRC Press, 2001.
- [30] H. Lee, S. Park, D. Park, S. H. Hahm, J. H. Lee, and J. H. Lee, "Nanometer-scale gap control for low voltage and high current operation of field emission array," *J. Vac. Sci. Technol. B, Microelectron. Process. Phenom.*, vol. 16, no. 2, pp. 762–764, Mar. 1998.
- [31] J. Wöbbeler, G. Pfeifer, and M. Hietschold, "Parasitic charging of dielectric surfaces in capacitive microelectromechanical systems (MEMS)," *Sens. Actuators A, Phys.*, vol. 71, no. 1/2, pp. 74–80, Nov. 1998.
- [32] A. Ni, D. Sherman, R. Ballarini, H. Kahn, B. Mi, S. M. Phillips, and A. H. Heuer, "Optimal design of multilayered polysilicon films for prescribed curvature," *J. Mater. Sci.*, vol. 38, no. 20, pp. 4169–4173, Oct. 2003.
- [33] H. Kahn, R. Ballarini, R. L. Mullen, and A. H. Heuer, "Electrostatically actuated failure of microfabricated polysilicon fracture mechanics specimens," *Proc. R. Soc. Lond. A, Math. Phys. Sci.*, vol. 455, no. 1990, pp. 3807–3823, Oct. 1999.
- [34] K. Abbas, Z. C. Leseman, and T. J. Mackin, "A traceable calibration procedure for MEMS-based load cells," *Int. J. Mech. Mater. Des.*, vol. 4, no. 4, pp. 383–389, Dec. 2008.
- [35] W. C. Tang, M. G. Lim, and R. T. Howe, "Electrostatic comb drive levitation and control method," *J. Microelectromech. Syst.*, vol. 1, no. 4, pp. 170–178, Dec. 1992.



**Mohammad Naraghi** received the B.S. and M.S. degrees in civil engineering from Sharif University of Technology, Tehran, Iran, in 2002 and 2004, respectively, and the Ph.D. degree in aerospace engineering from the University of Illinois, Urbana.

He is currently a Postdoctoral Research Fellow in the Department of Mechanical Engineering, Northwestern University, Evanston, IL. His research interests include the mechanical behavior of nanostructures and the design and application of MEMS in nanomechanics.

Dr. Naraghi received from Sandia National Laboratories the first-place award for winning in the MEMS University Alliance Design Student Competition in the category "Characterization, Reliability and Nanoscale Phenomena," in 2007 and 2008. He is the recipient of the 2009 Roger A. Strehlow Memorial Award for his outstanding graduate research from the Department of Aerospace Engineering, University of Illinois.



**Ioannis Chasiotis** received the Diploma in chemical engineering from the Aristotle University of Thessaloniki, Thessaloniki, Greece, in 1996 and the M.S. and Ph.D. degrees in aeronautics from the California Institute of Technology, Pasadena, in 1998 and 2002, respectively.

He is an Associate Professor of aerospace engineering at the University of Illinois at Urbana-Champaign, Urbana, where he is also a Part-Time Faculty Member at the Beckman Institute for Advanced Science and Technology and an Affiliate of the Micro and Nanotechnology Laboratory. His research includes the experimental mechanics of thin films with applications to MEMS/NEMS and coatings, and the spatial and temporal mechanics of nanofibers and their composites.

Dr. Chasiotis has been the recipient of a Presidential Early Career Award for Scientists and Engineers (PECASE), a National Science Foundation Faculty Early Career Development (CAREER) Award, an Office of Naval Research Young Investigator Award, a Xerox Award for Faculty Research, the Founder's Prize from the American Academy of Mechanics, and the Charles Babcock Memorial Award from the California Institute of Technology. He is a member of the American Society of Mechanical Engineers, Materials Research Society, and Society for Experimental Mechanics.